Exp Fluids (2009) 46:577–596
DOI 10.1007/s00348-008-0583-4

RESEARCH ARTICLE

The effect of roughness on separating flow over two-dimensional hills

J. B. R. Loureiro · A. S. Monteiro · F. T. Pinho · A. P. Silva Freire

Received: 28 February 2008 / Revised: 10 October 2008 / Accepted: 16 October 2008 / Published online: 11 December 2008

Abstract Two new experimental data sets for turbulent flow over a steep, rough hill are presented. These include detailed laser Doppler anemometry measurements obtained at the separation and reattachment points and, in particular, within the reverse flow region on the lee side of the hill. These results allow the development of a new parametrization for rough wall boundary layers and validate the use of Stratford's solution for a separating rough flow. The experiments were conducted in a water channel for two different Reynolds numbers. In the first set of rough wall experiments, the flow conditions and the hill shape are similar to those presented in Loureiro et al. (Exp. Fluids, 42:441–457, 2007a) for a smooth surface, leading to a much reduced separation region. In the second set of experiments, the Reynolds number is raised ten times. The region of separated flow is then observed to increase, but still to a length shorter than that recorded by Loureiro et al. (Exp. Fluids, 42:441–457, 2007a). Detailed data on mean velocity and turbulent quantities are presented. To quantify the wall shear stress, global optimization algorithms are used. The merit function is defined in terms of a local solution that is shown to reduce to the classical law of the wall far away from a separation point and to the expression of Stratford at a separation point. The flow structure at the separation point is also discussed.

J. B. R. Loureiro (✉) · A. S. Monteiro · A. P. Silva Freire
Mechanical Engineering Program (PEM/COPPE/UFRJ),
C.P. 68503, Rio de Janeiro 21945-970, Brazil
e-mail: jbrloureiro@mecanica.coppe.ufrj.br;
jbrloureiro@gmail.com

J. B. R. Loureiro
Scientific Division, Brazilian National Institute of Metrology (INMETRO), Rio de Janeiro, Brazil

F. T. Pinho
Universidade do Minho, Largo do Paço, 4704-553 Braga, Portugal

F. T. Pinho
Centro de Estudos de Fenómenos de Transporte,
Faculdade de Engenharia da Universidade do Porto,
Rua Dr. Roberto Frias s/n, 4200-465 Porto, Portugal

1 Introduction

Separating flow over rough terrain is a central research theme in micrometeorology. When the shape of a hill is steep enough to provoke flow separation, the resulting changes in the pressure field are often significantly large to make them the dominant effect on drag prediction. In relevant problems such as the dispersion of atmospheric pollutants, the sitting of wind turbines and even the large-scale forecast of weather and climate, the determination of the onset and extent of separated flow regions is an issue of utmost importance.

The separation of a flow from a solid wall can be simply explained in terms of the counterplay of the convection and diffusion of vorticity within the boundary layer. In regions where the flow is strongly retarded, the convective effects remove vorticity from the boundary at a lower rate than the feeding rate of vorticity from the upstream flow. Therefore, for the velocity outside the boundary layer to decrease downstream, the vorticity generated at the wall must have the opposite sense of rotation (negative vorticity). Provided the generation of negative vorticity at the wall is sufficiently large to overcome the effects of diffusion of positive vorticity towards the wall, a reverse flow region develops over the wall. This elegant interpretation of flow separation is given by Lighthill (1986).

For turbulent flow, the rates of diffusion increase, implying that much larger adverse pressure gradients can be withstood before separation occurs. Increasing the rate of turbulent diffusion by surface roughness is a manner of delaying or even preventing separation. The qualitative role of wall roughness on flow separation has been abundantly reported in the literature in connection with the so-called drag crisis. Unfortunately, no comprehensive theory—with clear and simple applicable rules—on rough wall turbulent separation has emerged.

One important objective of the present work is to carry out a detailed experimental study of separating flow over rough, steep hills. These experimental results are then used to verify the applicability of scaling laws for the various flow regions. Two new rigorous sets of data are introduced to characterize the sensitivity of separation to wall roughness. In particular, the measurements include detailed results obtained at the separation and reattachment points and in the reverse flow region on the lee side of the hill. This is an aspect of the experimental investigation of flow over hills that has always been known to be deficient. Regarding the first data set, the flow conditions and hill shape of Loureiro et al. (2007a, b) for flow over a smooth surface are repeated for flow over a rough wall. As it turns out, the position of the separation point is slightly displaced downstream and the extent of separated flow is much reduced. Regarding the second data set, the flow Reynolds number is increased ten fold, but the hill shape and roughness are kept identical to the first set. The separation point is observed to be pushed farther downstream, yielding a region of reverse flow significantly enlarged in comparison to the lower Reynolds number set, but still shorter than that observed for flow over a smooth surface. All experiments were conducted in a water channel using a two-dimensional laser Doppler velocimeter to characterize in detail the regions of attached and reversed flow.

The present contribution is centered on two major concerns: (1) to promote the present extensive and high quality data base for flow in the lee of the hill (which are rather rare) and (2) to discuss the flow structure in the vicinity of a separation point. In addition, this work complements the smooth-surface flow data set of Loureiro et al. (2007a, b), throwing further light on the understanding of separating turbulent boundary layer flows over steep hills under a variety of surface conditions. For this purpose, complementary to two-component mean flow quantities, some higher-order statistics and skin-friction distributions are also presented. Data for the shear and normal components of the Reynolds stress tensor and for the skewness and flatness factors of the streamwise and vertical velocity fluctuations are thoroughly investigated. Some of these quantities convey structural information about the flow field and can be used to disclose the behaviour of boundary layers under the dominating effects of topographic changes.

Early experimental studies on wind tunnel flows over rough hills have sought data for locations at or upwind of the hill top but not in the wake. The main concerns were usually the characterization of flow speedup and the extent of separated flow. The motivation then was clear, linear theories (see, e.g., Jackson and Hunt 1975; Sykes 1980; Hunt et al. 1988) naturally demanded data on flow over two-dimensional low hills for model validation. Since mean velocity and turbulence measurements were conducted in wind tunnel facilities using hot- and pulsed-wire anemometers, very often only qualitative information was given on some characteristics of separated flow. Typical examples are the works of Arya et al. (1986) and of Britter et al. (1981).

More recently, the modelling emphasis has shifted to numerical schemes that consider the full non-linear equations of motion. The impressive advances in computing power have implied that simulations previously considered unaffordable have now become routine. Turbulence models ranging from first-order eddy-viscosity through second order closure schemes have been implemented and tested against a variety of flow conditions (Castro and Apsley 1997; Ying and Canuto 1997; Hewer 1998; Ross et al. 2004). Even works on much more demanding techniques such as large-eddy simulations can nowadays be regularly found in the literature (Brown et al. 2001; Allen and Brown 2002; Iizuka and Kondo 2004).

This plethora of numerical data should naturally be accompanied by reference experimental data. Unfortunately, this is not the case if we consider the separated flow region on the lee of a hill. The existence of regions of reverse flow narrows down the choice of experimental techniques to those that can discriminate flow direction. Typical choices are then pulsed-wire anemometry (HWA), laser Doppler anemometry (LDA) and particle image velocimetry (PIV). The works of Kim et al. (1997) (HWA), of Ishihara et al. (2001) (HWA) and of Ross et al. (2004) (LDA) present wind-tunnel studies on the flow over steep hills. However, in none of these works, for example, are values of the friction velocity given.

2 Theoretical background

2.1 Attached and separated flows over smooth walls

For attached flows over smooth surfaces, the asymptotic diagram of the turbulent boundary layer has been shown to depend on two characteristic length scales: the thickness of the inner, viscous region ($\hat{\delta} = \nu/u_*$, $u_* = \sqrt{\tau_w/\rho}$) and the thickness of the outer, defect region (δ). In fact, the

classical two-layered asymptotic theories of Yajnik (1970), Mellor (1972) and Bush and Fendell (1972) are rendered true provided a small wake velocity deficit occurs. Close to a separation point, where the wake velocity is large and u_* is identical to zero, a new local scaling velocity needs to be considered. Goldstein (1948) showed this scaling velocity to be u_{pv} (= $((\nu/\rho)\ \partial_x p)^{1/3}$) and the local velocity profile to assume a parabolic shape.

Under large pressure gradients, the velocity profile must be sharply curved at the wall. Since in the immediate vicinity of the wall, the inertial and turbulent terms in the Reynolds averaged Navier–Stokes equations are negligible, the viscous forces must be comparable with the pressure forces, however sharp the latter might be.

Hence, the following local approximate equation applies

$$0 = -\rho^{-1}\partial_x p + \nu\partial_z^2 u. \tag{1}$$

A double integration gives Goldstein's solution

$$u = (2\nu\rho)^{-1}(\partial_x p)z^2 + (u_*^2\nu^{-1})z. \tag{2}$$

In Loureiro et al. (2007a), Eq. 2 was shown to hold over the entire flow region. In particular, it was used to find u_* and $\partial_x p$ in regions of reversed flow (see, e.g., Fig. 10). Please note that as $\partial_x p \to 0$, a linear solution is obtained.

Farther away from the wall, a new distinct region can be identified where the turbulent term gains in importance as compared to the viscous term. The existence of such region has been thoroughly discussed by Sychev and Sychev (1980), Durbin and Belcher (1992) and Cruz and Silva Freire (1998). Hence, the local approximate equation reduces to

$$\partial_z\overline{u'w'} = -\rho^{-1}\partial_x p. \tag{3}$$

A first integration gives

$$-\overline{u'w'} = (\rho^{-1}\partial_x p)z + u_*^2. \tag{4}$$

Equation (4) provides a second method to find u_* and $\partial_x p$ through the direct measurement of $\overline{u'w'}$. In particular, in regions where $\partial_x p \to 0$, a region of constant $\overline{u'w'}$ should be identified. At a separation point, where $u_* = 0$, the behaviour of $\overline{u'w'}$ in the fully turbulent region must be linear.

To further integrate Eq. 4 the turbulent term needs to be modelled. The simplest approach is to consider the eddy viscosity hypothesis together with the mixing-length model. Then, Eq. 4 can be written as

$$(\varkappa z)^2(\partial_z u)^2 = (\rho^{-1}\partial_x p)z + u_*^2, \tag{5}$$

with $\varkappa = 0.4$ (von Karman's constant).

Two particular cases are admitted by Eq. 5. In regions where $\partial_x p \to 0$, the corresponding solution is the logarithmic law of the wall (Prandtl's solution),

$$u = \varkappa^{-1}u^* \ln z + A. \tag{6}$$

At a separation point ($u_* = 0$), the solution becomes Stratford's (1959) solution

$$u = 2\varkappa^{-1}(\rho^{-1}\partial_x p)^{1/2}z^{1/2} + B. \tag{7}$$

The above equations define a third method to determine u_* and $\partial_x p$. Plots of u against z and $z^{1/2}$ can be used to find u_* and $\partial_x p$ from the slopes of Eqs. 6 and 7, respectively, since, we have seen, $\varkappa = 0.4$.

The general solution of Eq. 5 has been given in Cruz and Silva Freire 1998, as

$$u = 2\varkappa^{-1}\sqrt{\Delta_w} + \varkappa^{-1}u_* \ln\left(\left(\sqrt{\Delta_w} - u_*\right)/\left(\sqrt{\Delta_w} + u_*\right)\right) + C, \tag{8}$$

with $\Delta_w = \rho^{-1}\ \tau_w + \ (\rho^{-1}\ \partial_x p)\ z$.

In Loureiro et al. (2007b), Eq. 8 was used as a lower boundary condition in the numerical simulation of separating flow over a steep, smooth hill. The formulation was shown to perform well in regions of attached and reversed flow. Note that under the appropriate limit processes, Eq. 8 reduces to Eqs. 6 and 7. Loureiro et al. (2007b) have also analyzed in their study the formulations of Mellor (1966) and Nakayama and Koyama (1984).

2.2 Attached and separated flow over rough walls

For flows over fully rough surfaces, the very complex flow patterns that develop around the roughness elements prevent the lower boundary condition to be specified directly on the contour of the roughness elements. The standard procedure to avoid this problem is to specify the lower boundary condition at some distance from the wall in a region where the flow statistics are spatially homogeneous.

Therefore, trivially defined parameters for flow over a smooth wall need a much deeper consideration for flow over a rough surface. The friction velocity, u_*, and the wall pressure gradient, $(\partial_x p)_w$, are not defined around the contour of the roughness elements, but, instead, at some distance from the wall where the complex flow around the individual roughness elements is not apparent anymore. Under particular conditions, provided pressure taps can be fitted around roughness elements, the method of Perry et al. (1969) can be used to find u_*. The local pressure gradient, however, has to be found from chart methods based on the local distribution of mean velocity. Note that both methods are highly inaccurate in regions of separated flow since the pressure around the roughness elements attains very low values and the existence of a logarithmic profile—a required condition for the use of chart methods—may not be granted.

The complete destruction of the viscous sub-layer by the roughness elements means that the solution of Goldstein (Eq. 2) does not hold anymore and characteristic scales dictated by the roughness itself must be brought into the problem.

For attached flows, a common practice is to re-write Eq. 6 as

$$u^+ = \varkappa^{-1} \ln((z-d)/z_0), \tag{9}$$

where z is distance from the bottom of the roughness elements (see Fig. 1).

Thus, the specification of the lower boundary condition on rough walls is considered to depend on two characteristic scales: the roughness length, z_0, and the displacement height, d. Unfortunately, neither z_0 nor d are directly measurable quantities, but they depend on the large number of geometric parameters that are needed to characterize the roughness. In fact, depending on the way roughness elements are packed together these scales might also vary with the flow properties. Classical discussions on this problem are introduced in the papers of Perry and Joubert (1963) and Perry et al. (1969). For a recent review on the subject, readers are referred to Snyder and Castro (2002) and Castro (2007).

The solution of Cruz and Silva Freire (1998)—Eq. (8)—is valid for the fully turbulent region of the flow; as such, all details regarding the wall roughness must enter the problem through the integration parameter C. In general, in adverse pressure gradient flows, C should depend on τ_w, $\partial_x p$ and z_0. Also, any proposed functional form for C must be consistent with the logarithmic and root-squared solutions under the corresponding limits $\tau_w \gg (\partial_x p)\, z$ and $\tau_w \ll (\partial_x p)\, z$.

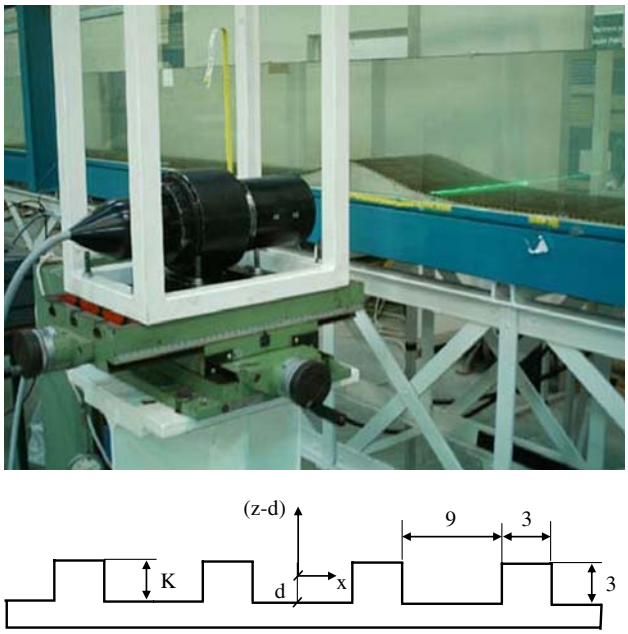

Fig. 1 Illustration of model hill and details of rough surface. Dimensions are in mm. K = height of the roughness elements, d = displacement height, z = distance from the bottom of the roughness elements, $z_T = z - d$

To recover Eq. 9 from Eq. 8 under the condition $\tau_w \gg (\partial_x p)\, z$, C has to be specified according to

$$C = \varkappa^{-1} u_* \left[\ln\left(4u_*^2/((\rho^{-1}\partial_x p) z_0)\right) - 2\right]. \tag{10}$$

The implication is that attached and separated turbulent flows over rough surfaces can be locally represented in the fully turbulent region by

$$u = 2\varkappa^{-1}\sqrt{\Delta_w} + \varkappa^{-1} u_* \ln\left((\sqrt{\Delta_w} - u_*)/(\sqrt{\Delta_w} + u_*)\right) + \varkappa^{-1} u_* \left[\ln\left(4u_*^2/((\rho^{-1}\partial_x p) z_0)\right) - 2\right], \tag{11}$$

with $\Delta_w = \rho^{-1}\ \tau_w + \ (\rho^{-1}\partial_x p)\ z_T$ and $z_T = z - d$.

This equation will be thoroughly tested in the following sections. However, before we do this, a few comments are in order.

We have indicated through the previous remarks how relevant wall shear stress data are for the validation of asymptotic theories. For neutral, attached flows the velocity field is known to exhibit a logarithmic solution that scales with the friction velocity, $u_* (= \sqrt{\tau_w/\rho})$. At a separation point, the velocity field follows a square-root behaviour, being scaled by u_{pv} $(= ((\nu/\rho)\partial_x p)^{1/3})$. This change in reference velocity has a profound influence on the asymptotic structure of the flow, and is very difficult to accommodate into a single theoretical framework (Cruz and Silva Freire 1998). Data on the local behaviour of u_* and u_{pv} are then largely coveted by researchers for they permit the construction and validation of rational approaches to the problem.

Unfortunately, the friction velocity is a parameter very difficult to quantify. Loureiro et al. (2007a) have commented on the various possible direct and indirect measurement techniques for flow over a smooth wall. In particular, the difficulties associated with measurements over curved surfaces were discussed. As it turns out, wall shear stress was evaluated by fitting procedures that resorted to the near wall behaviour of the velocity profile.

Graphical methods have been used abundantly on the estimation of u_*. For external boundary layers over rough surfaces this seems to be the only plausible choice together with estimations based on the shear stress profile. Of course a major drawback of these techniques is the built-in assumptions concerning the nature of the velocity and shear stress profiles—considered logarithmic and nearly uniform near the wall, respectively. However, as we have just seen, close to a separation point, adjustments have to be made to Eq. 9 so that coherent results are obtained. Therefore, the importance of Eq. 11 cannot be overstated. This equation generalizes the log- and $z^{1/2}$-laws furnishing

a method to find the two unknown parameters u_* and $(\rho^{-1}\,\partial_x p)$ from given mean velocity profiles. This requires that z_0 and d in Eq. 11 have to be known parameters, which must be determined a priori and independently from the undisturbed velocity field. To find u_* and $(\rho^{-1}\,\partial_x p)$, global optimization algorithms can then be applied onto Eq. 11.

Numerical algorithms for constrained nonlinear optimization can be categorized into gradient based methods and direct search methods. Gradient-based methods use first derivatives (gradients) or second derivatives (Hessians). Direct search methods do not use derivative information and tend to converge more slowly, but can be more tolerant to the presence of noise in the function and constraints. Typically, both types of algorithms only build up a local model of the problems and they insist on a certain decrease of the objective function, or on a decrease of a merit function which is a combination of the objective and constraints, to ensure convergence of the iterative process. If convergent, such algorithms will only find local optima and for that reason are called local optimization algorithms.

Global optimization algorithms, on the other hand, attempt to find the global optimum, typically by allowing decrease as well as increase of the objective/merit function and consequently are computationally more expensive. Here, four direct search methods were used to determine the parameters of interest u_* and $(\rho^{-1}\,\partial_x p)$: nelder mead, differential evolution, simulated annealing and random search. When all four methods furnished consistent results, with accuracy down to the sixth decimal fraction, the search was stopped.

3 Experiments

3.1 Water channel, model hill and roughness

The experiments were carried out in the same water channel described by Loureiro et al. (2007a, b). The channel is in the Hydraulics Laboratory of the Civil Engineering Department of the University of Oporto, having a total length of 17 m. The cross section area is 0.40 m wide by 0.60 m high, and the sides and bottom of the channel are made of glass and acrylic, respectively.

The water pumping system can reach a top volumetric flow rate of 150 l/s. Two pumps are used to keep the maximum flow rate variation to within ±0.8%. Screens and filters are used to stabilize the flow and suppress any excessive level of turbulence. They also control the size of particles in suspension in the water. A magnetic flowmeter is used to measure the flow rate with an uncertainty of 0.001 l/s. The water level is controlled through a vertical steel gate. In this work, two flow rates were used: 2.65 and 26.76 l/s.

The hill model was placed 12 m downstream of the channel entrance. A Witch of Agnesi profile shaped the hill according to the following equation

$$z_H = H_1\left[1 + (x/L_H)^2\right]^{-1} - H_2, \tag{12}$$

where H ($=H_1-H_2$) (=60 mm) is the hill height and L_H (=150 mm) is the characteristic length representing the distance from the crest to the half-height point.

The roughness elements consisted of rigid rubber strips 3 mm wide by 3 mm high that were spaced by 9 mm. The rough surface extended from 1.5 m upstream of the hill top to 1.5 m downstream. The geometric details of the surface are given in Fig. 1; K is used to denote the height of the roughness elements, d the displacement height, z the distance from the bottom of the roughness elements and $z_T = z - d$.

Illustrations of the hill and of the roughness are shown in Fig. 1.

Measurements were made on the channel centerplane at the positions illustrated in Fig. 2. Regarding the lower Reynolds number data set—RSA—11 stations are investigated to discriminate the regions of attached and reversed flow. As for the higher Reynolds number data set—RSB—12 measuring stations are distributed along the flow over rough surface. The measuring positions were defined through a flow visualization study. The particular concern

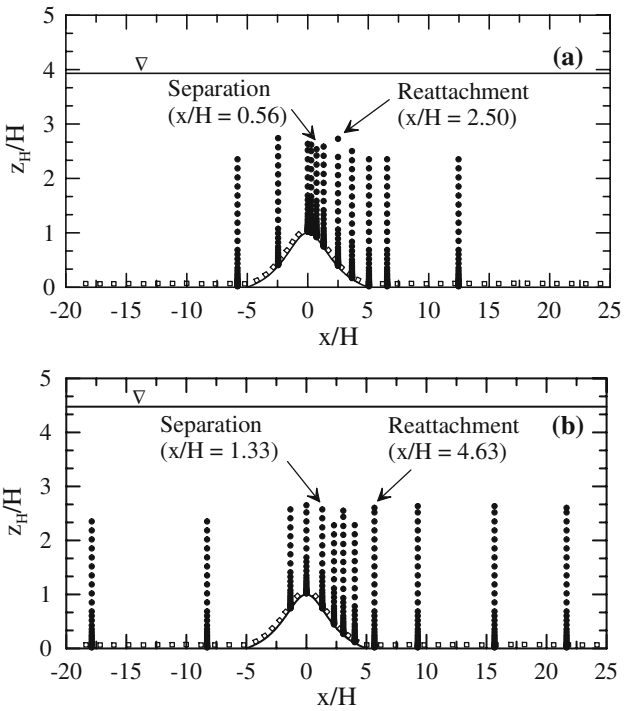

Fig. 2 Location of measuring stations. **a** lower Reynolds number data set (RSA, $R_\delta = 4{,}425$), **b** higher Reynolds number data set (RSB, $R_\delta = 31{,}023$). Note the origin of the coordinate system (x, z_H)

was to characterize well the regions of separated ($\tau_w = 0$) and reversed flow. For this reason, measurements were not carried out exactly at the same position.

3.2 Instrumentation

A two-component Dantec laser-Doppler anemometry system using an Ar-ion tube laser was operated in the forward scatter mode to measure the mean and fluctuating velocity fields. A Bragg cell unit was used to introduce an optical-electronic shift of 40 MHz. That was necessary to resolve the direction of the flow field and give correct measurements of near-zero mean velocities. The beams were made to pass through a series of conditioning optical elements to achieve a small measurement volume and to improve the optical alignment. A front lens with 500 mm focus length was mounted on the probe to accurately position the measurement volume on the centerline of the channel. Before being collected by the photomultipliers, the scattered light was made to pass through interference filters of 514.5 and 488 nm, so that only the green and blue lights were received on each photomultiplier, respectively. Table 1 lists the main characteristics of the laser-Doppler system used. The signals from the photomultipliers were band-pass filtered and processed by a burst spectrum analyzer operating in the single measurement per burst mode. A series of LDA biases were avoided by adjusting the strictest parameters on the data processor. The level validation and the signal to noise ratio were eight and five, respectively. For simultaneous measurements of longitudinal and vertical velocities, a coincidence window of 5,000 μs was used. For the statistics at each point, 20,000 samples were considered.

Typical uncertainties associated with the mean velocity data—U, W—are below 0.2% of the free stream velocity, U_δ, except in regions of reverse flow, where they increase to about 0.3%. Regarding the Reynolds stress components $\overline{u'u'}$, $\overline{w'w'}$, $\overline{u'w'}$ uncertainties were estimated to be 2.3, 1.8 and 4.2% of the square of the friction velocity of the undisturbed flow, respectively, increasing to 3.8, 3.5 and 6.9% in the reverse flow region. For the skewness and flatness factors for the longitudinal and vertical velocity fluctuations, local relative uncertainties of 3.5 and 13.9% were associated with $S_u(=\overline{u'^3}/(\overline{u'^2})^{3/2})$, $S_w(=\overline{w'^3}/(\overline{w'^2})^{3/2})$, and $F_u(=\overline{u'^4}/(\overline{u'^2})^2)$, $F_w(=\overline{w'^4}/(\overline{w'^2})^2)$, respectively.

4 Experimental results

4.1 General flow pattern

To place the present results into the perspective of the results of Loureiro et al. (2007a), we begin this section by comparing in Fig. 3 the streamlines of all three experimental conditions: the smooth wall data of Loureiro et al. (2007a)—SS—and the two new data sets of flow over rough surface—RSA and RSB. These streamlines were obtained through an interpolation of the measured velocity profiles so that they configure an approximation of the observed flow field.

Table 1 Main characteristics of the laser-Doppler system

Wavelength	514.5 nm (green) 488 nm (blue)
Half-angle between beams	1.604°
Fringe spacing	9.2 μm (green) 8.7 μm (blue)
Beam spacing	28 mm
Beam diameter	2.2 mm
Dimensions of the measurement volume	
Major axis	5.31 mm (green) 5.04 mm (blue)
Minor axis	149.0 μm (green) 141.0 μm (blue)

The sensitivity of flow separation to the wall roughness is apparent. In fact, the position of the separation and reattachment points can be promptly identified in Fig. 3. The exact location of these points is explicitly quoted in Table 2. The largest region of reverse flow is observed to occur over the smooth hill (Fig. 3a). Flow with the same oncoming external mean velocity, but over a rough wall is shown in Fig. 3b. The separation point is slightly displaced downstream and the region of reverse flow is much reduced. An increase in external mean velocity of about ten fold moves the separation point farther downstream and causes the region of reverse flow to enlarge (Fig. 3c).

4.2 Undisturbed flow conditions

Loureiro et al. (2007a) have shown that the mean velocity profiles at stations far upstream of the hill compare to within 5% with the mean velocity profile in the absence of the hill at station $x/H = 0$. The same percentage was observed to hold for the two flows over a rough surface. For this reason, the undisturbed flow properties will be here characterized in terms of the far-upstream velocity profiles.

To find u_*, d and z_0 two methods were used: the graphical method of Perry et al. (1969) and the hypothesis of Prandtl (1925) that across the wall layer the total shear stress deviates just slightly from the wall shear stress.

In the first method, the raw undisturbed velocity profiles were subtracted by a small value (e.g. 0.1 mm) from their distance to the wall. Then, a global optimization algorithm was used to find the best logarithmic fit. This process was progressively repeated—using the same subtraction

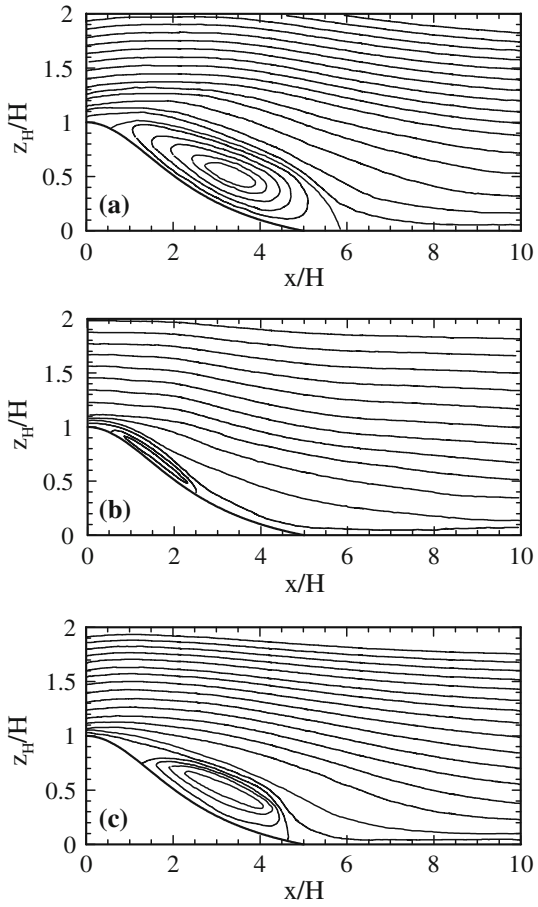

Fig. 3 General pattern of reverse flow region. **a** SS, **b** RSA, **c** RSB

Table 2 Position of separation and reattachment points in x/H units

Conditions	Separation	Reattachment	Length
SS	0.50	5.80	5.30
RSA	0.56	2.50	1.94
RSB	1.33	4.63	3.30

step—until the curve with the best statistics could be identified.

Characteristic properties of the undisturbed profiles are listed in Table 3, together with the corresponding characteristics of the undisturbed profile of Loureiro et al. (2007a) for a smooth surface.

To evaluate the two-dimensionality of the flow, mean velocity measurements were obtained in x–z planes located 5 cm to either side of the channel centerplane. When the hill was not in place, the results showed a variation of 2% in relation to measurements taken at the channel centerplane. In the presence of the hill, such differences in velocity measurements were of about 3%.

4.3 Longitudinal mean velocity profiles

4.3.1 General analysis and the applicability of Eq. 11

The applicability of Eq. 11 to attached as well as separated flows is illustrated in Figs. 4, 5 and 6, where it is illustrated by the solid lines.

For both conditions, RSA and RSB, the overall agreement between the theoretical predictions, represented by the solid lines, and the experimental data was very good upstream of and at the hill top (Fig. 4). In particular, note the very well defined logarithmic region for position $x/H = -17.87$ and $x/H = -5.8$. These profiles correspond to the limit case $\tau_w \gg (\partial_x p)$, when Eq. 11 must reduce to Eq. 9.

Some differences in speed-up behaviour between the present experiments and the smooth wall data set of Loureiro et al. (2007a) can be noted. In Loureiro et al. (2007a) the flow accelerates to about 1.3 U_δ on the hill top, exhibiting an almost uniform external flow behaviour. For condition RSA, this tendency is repeated; in particular, the flow also speeds up to 1.3 U_δ. However, for condition RSB, the velocity profile on the hill top is less full, accelerating in the near wall region to 1.05 U_δ and in the external region to 1.2 U_δ. Despite the distinctions in flow behaviour, Eq. 11 captures very well the speed-up variations.

Predictions on the lee side of the hill are investigated in Fig. 5. The small region of reverse flow for condition RSA is evident. The flow is clearly attached at $x/H = 0.29$. At the next two locations, only the first three ($x/H = 0.73$) and four ($x/H = 1.31$) points near the wall show negative velocities. Farther out the velocity profiles are still relatively full, with small velocity deficits. For the higher Reynolds number flow (condition RSB), the separation point is located at $x/H = 1.33$. At this station, the three measured points nearest to the wall are well aligned vertically, an indication that flow reversal is imminent. At stations $x/H = 2.3$, 3.06 and 4.03 the vertical extent of reverse flow appears to be approximately limited by $z_T \leq 0.25$.

The curve fits given by Eq. 11 work very well for all measuring positions, for both RSA and RSB conditions. However, it must be pointed out that in regions of reverse flow, the present results have shown that a very small value of z_0 must be used in the calculations. Here, we have considered $z_0 = \text{ord}(10^{-6})$ m. This finding is a mere reflection that in regions of dead fluid the wall roughness details must not be relevant in drag predictions.

Far downstream, the perturbation effects of the hill spread out promoting a return of the velocity profile to equilibrium conditions. In the present experiment, this has not been observed in either condition RSA or RSB (Fig. 6). Equation 11, nonetheless, does provide a good representation to the near wall flow.

Table 3 Properties of undisturbed profile

Property	SS	RSA	RSB
Station x/H	−12.5	−5.8	−17.87
Boundary layer thickness (δ, mm)	100	90	100
Displacement thickness (δ_1, mm)	09	16	15
Momentum thickness (δ_2, mm)	6.6	10.5	10.2
External velocity (U_δ, ms^{-1})	0.0482	0.0497	0.3133
Friction velocity u_* (ms^{-1}) (Clauser)	0.0028	0.0047	0.0204
Friction velocity u_*, (ms^{-1}) ($\overline{u'w'}$)	0.0023	0.0043	0.0225
Displacement height (d, mm)	0.0	2.1	2.0
Roughness length (z_0, mm)	0.08	0.83	0.33
Longitudinal velocity fluctuations at $z/\delta = 0.05$ ($\sqrt{\overline{u'u'}}/u_*$)	2.50	1.71	1.89
Transversal velocity fluctuations at $z/\delta = 0.08$ ($\sqrt{\overline{w'w'}}/u_*$)	0.83	1.44	1.67
Reynolds number (R_δ)	4,772	4,425	31,023
Reynolds number (R_{z_0})	0.22	3.88	6.65

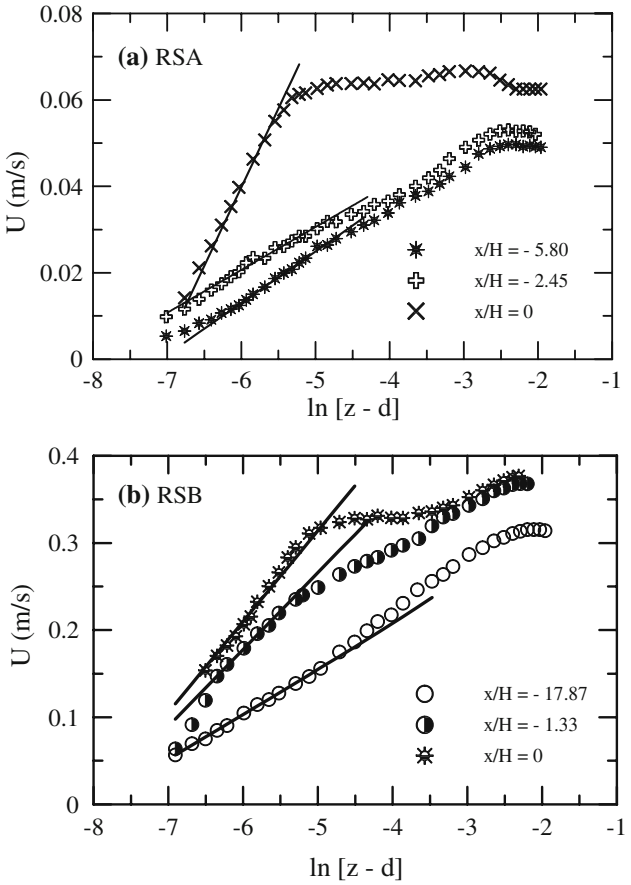

Fig. 4 Mean velocity profiles upstream of and on the hill top, x-component. z = distance from the bottom of the roughness elements, d = displacement height. *Solid lines* denote Eq. 11. **a** RSA, **b** RSB

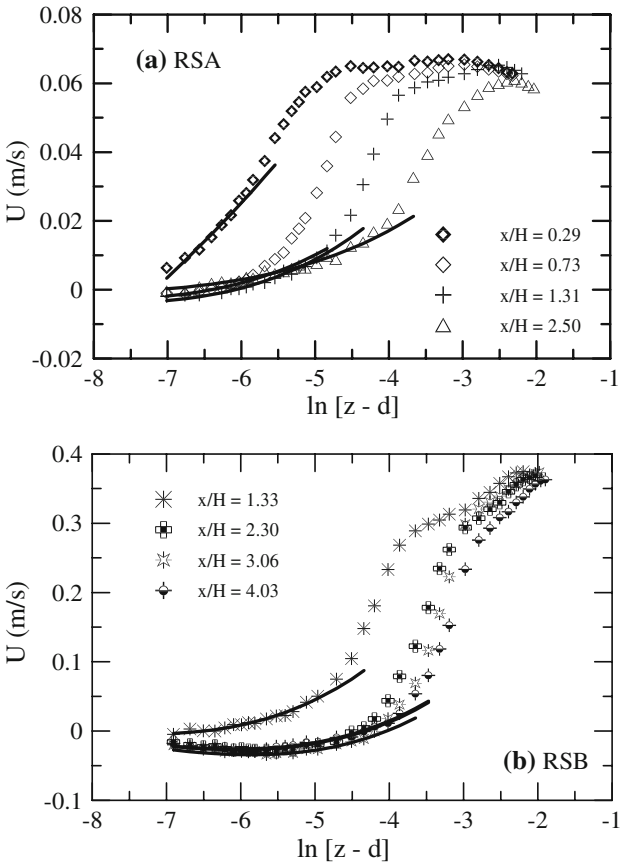

Fig. 5 Mean velocity profiles on the lee side of hill, x-component. z = distance from the bottom of the roughness elements, d = displacement height. *Solid lines* denote Eq. 11. **a** RSA, **b** RSB

4.3.2 Stratford's solution

For steady separating turbulent boundary layers, a set of definitions has been advanced in the literature to characterize the different states of detachment. The following convention is normally used: ID = incipient detachment (existence of backflow 1% of time), ITD = intermittent transitory detachment (backflow 20% of time), TD = transitory detachment (backflow 50% of time), D = detachment (position where $\tau_w = 0$). Experimental evidence suggests

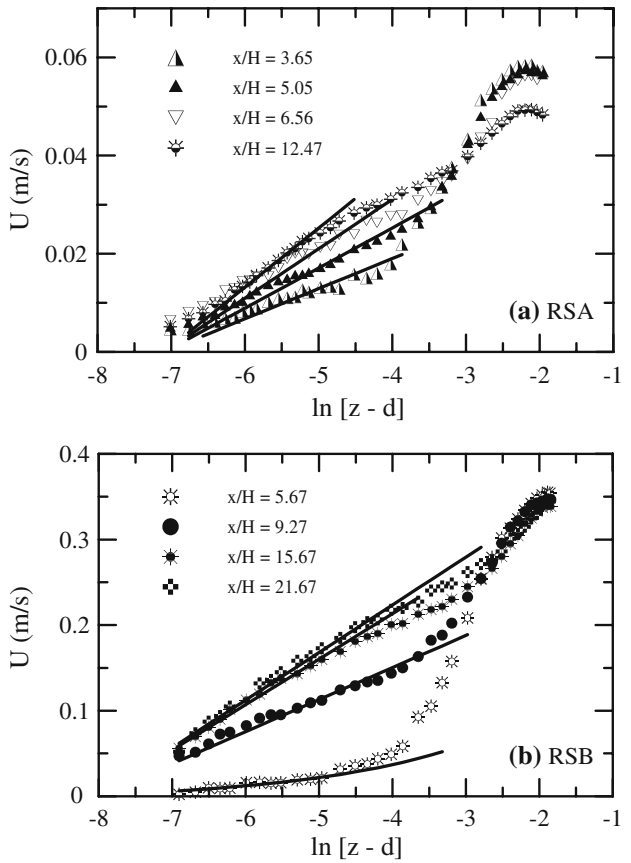

Fig. 6 Mean velocity profiles downstream of the separation bubble, x-component. z = distance from the bottom of the roughness elements, d = displacement height. *Solid lines* denote Eq. 11. **a** RSA, **b** RSB

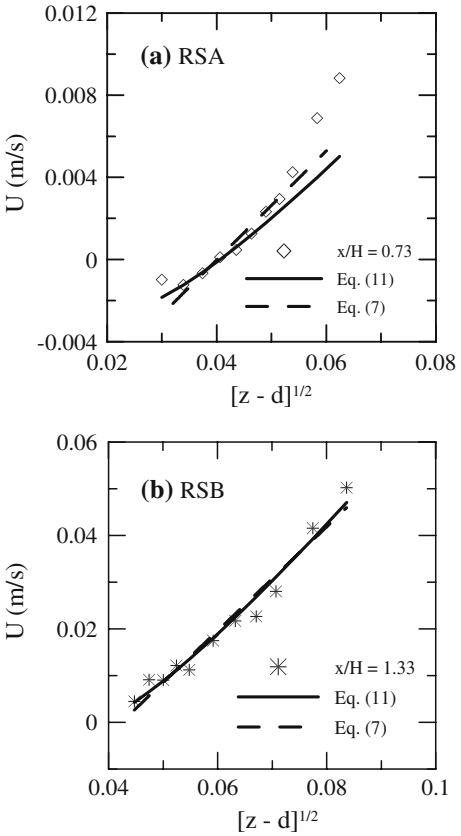

Fig. 7 Stratford's solution. **a** RSA, **b** RSB

that TD and D are located at the same point. Therefore D, a steady parameter, is defined in terms of TD, an intermittent transitory parameter (Simpson 1996). For this reason, determining the exact wall position where flow separation occurs is not an easy task.

In the present work, the two possible profiles where the condition of detachment can be identified are profiles $x/H = 0.73$ (RSA) and 1.33 (RSB). They are shown in Fig. 7 together with curve fits given by Eqs. 7 and 11. Clearly, the velocity profile at $x/H = 0.73$ does not follow the $z^{1/2}$-law. In fact, the negative value of u_* indicates this profile to be in the region of reverse flow. The profile at $x/H = 1.33$, on the other hand, is very well represented by Eqs. 7 and 11, which are almost coincident. The verification of Stratford's solution for a separating flow over a rough wall is an important result that is rarely discussed in the literature.

4.4 Vertical mean velocity profiles

For both flow conditions, the vertical mean velocity profiles on the upstream side of the hill (figures are not shown for conciseness) are dominated by the effects of change in elevation; W increases to values of the order of 0.15 and 0.2 U_δ for the conditions RSA and RSB, respectively. On the hilltop, the isolated effect of hill symmetry should reduce W to zero. For the SS condition, Loureiro et al. (2007a) have shown that the deflection of the near wall streamlines due to the large extent of separated flow on the lee side of the hill gives rise to very large values of W throughout z_T as compared with the undisturbed profiles. In particular, in the near wall region, Loureiro et al. (2007a) found $W \approx 0.08\ U_\delta$. The shallow separation bubble resulting from condition RSA, however, yields maximum values of $W\ (\approx\ 0.05\ U_\delta)$ at the hill top just for the first four measured points. Farther away from the wall, $W \approx 0.02\ U_\delta$. In contrast, condition RSB at $x/H = 0$ is strongly influenced by the separation bubble so that, for all values of z_T, $W \geq\ 0.06\ \ U_\delta$.

On the lee side of the hill, the flow deceleration and wall curvature results in large negative values of W outside the separation bubble for condition RSA; as x/H increases W becomes more negative, as shown in Fig. 8. However, the near wall values of W are dictated by the presence of the separation bubble so that they must be small. It is of interest to note the sharp variation in vertical velocity close

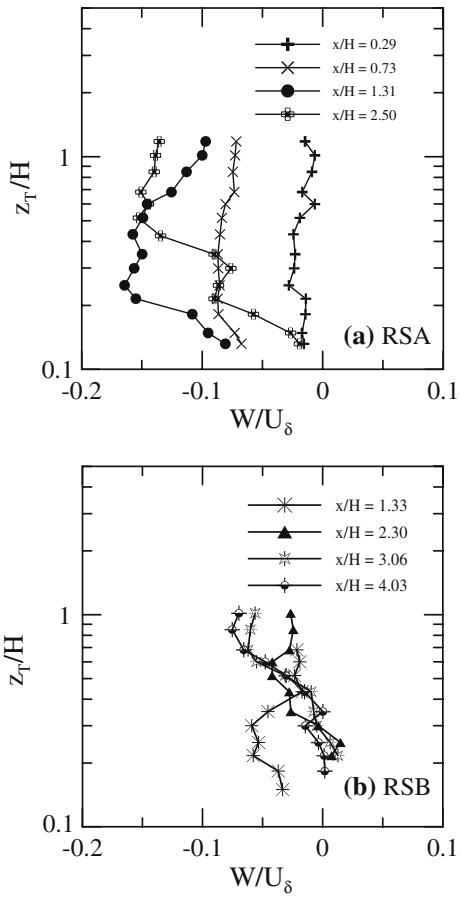

Fig. 8 Mean velocity profiles on the lee side of hill, z-component. $z_T = z - d$, z = distance from the bottom of the roughness elements, d = displacement height. **a** RSA, **b** RSB

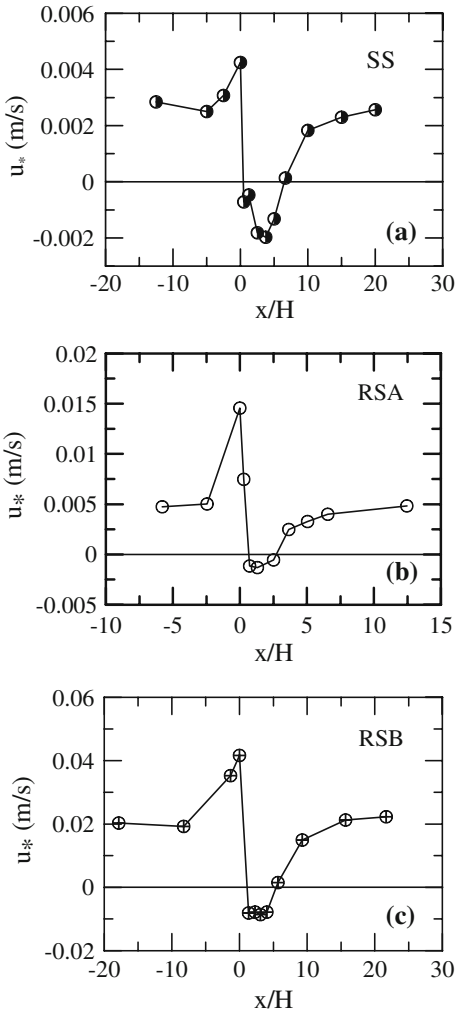

Fig. 9 The behaviour of u_* for all three flow conditions. **a** SS, **b** RSA, **c** RSB

to the wall for the profiles at $x/H = 1.31$ and 2.5. For condition RSB, W is negative at $x/H = 1.33$, an indication of the dominance of topographic effects at the separation point. At all other stations, W is positive but close to zero in the separation bubble and negative otherwise.

Further downstream of the hill, at stations $x/H = 12.47$ (RSA) and 15.66 (RSB), the vertical velocity profiles are nearly zero indicating that the remaining topographic effects are small. These are not shown here for conciseness.

4.5 Skin-friction results

The usefulness of Eq. 11 to find the wall shear stress is illustrated next.

The optimization process described in Sect. 2.2 and used in Sect. 4.3 naturally furnishes local values of u_* and $\partial_x p$ for given tabulated values of z versus u. Of course, this is true provided d and z_0 are known beforehand. For attached flow, we have mentioned that the undisturbed values of d and z_0 must be used (Table 3). In regions of reversed flow, d remained unchanged but z_0 was taken to be 10^{-6} m. Results for u_* are shown in Fig. 9 for both rough surfaces. Results concerning the smooth-wall flow, condition SS, have also been included for the sake of theory validation.

The agreement between results provided by Eq. 11 and the smooth wall data of Loureiro et al. (2007a) is accurate to within 3% even in the region of separated flow. Through the previously described optimization process, Eq. 11 can capture all the relevant friction velocity behaviour. The region of rise before the hill top, the position of the separation point, the length of the separated flow region, the return to equilibrium condition, these are features that are all well predicted by the present procedure.

The influence of wall roughness is also well modelled. The increase in the undisturbed values of u_* for conditions RSA and RSB as a function of the roughness and of the external flow Reynolds number are in accordance with estimation methods based on the classical law of the wall. The extent of separated flow is also very well predicted when compared with Fig. 3.

Table 4 Skin-friction velocity predictions at the separation point $x/H = 1.33$ (RSB condition)

Eq.	u_* (ms^{-1})	$\rho^{-1}\partial_x p$ (ms^{-2})
(4)	−0.0082626	0.095585
(7)	0.0	0.049461
(11)	−0.008088	0.088580

Table 4 shows the results for the estimation of u_* at the separation point $x/H = 1.33$ (RSB condition). Note that by definition Eq. 7 implies $u_* = 0$ and the fitting procedure yields $B = -0.047103$. The agreement between results given by Eqs. 4 and 11 is very good. The discrepancy exhibited by Eq. 7 results from the value of $\varkappa$ used, the canonical value 0.4.

4.6 Second moments

4.6.1 General analysis

The changes in turbulent second moments or Reynolds stresses are of particular importance. To understand the behaviour of turbulence, Kaimal and Finnigan (1994) consider indispensable the concepts of local equilibrium, rapid distortion and turbulence memory. In particular, they discuss the reaction of the Reynolds stresses to a combination of basic strains related to flow acceleration, curvature and shear. For a complete discussion on this topic, with access to a quick guide, the reader is referred to the original source.

Turbulence over a hill is also discussed by Britter et al. (1981). Two reference time scales are invoked to pose arguments: the advection time, T_a, that eddies spend to traverse the hill, and their Lagrangian time scale, the turnover time T_L. Along streamlines where $T_a \ll T_L$ the distortion of turbulent eddies by the mean flow is too fast to allow them to adjust to local strain rates. Vortex tubes can then just be compressed, expanded or rotated. In the external flow region, changes are fast enough to make rapid distortion a plausible consideration. In particular, at the hill top, external flow streamlines are simply compressed with no rotation of vortex elements. Citing Batchelor and Proudman (1954) and Townsend (1976), Britter et al. (1981) wrote

$$\frac{\overline{u'u'}(x,z)}{\overline{u'u'}(z_s)} = 1 - \frac{4\Delta u(x,z)}{5\ U_\delta(z_s)}, \tag{13}$$

$$\frac{\overline{w'w'}(x,z)}{\overline{w'w'}(z_s)} = 1 + \frac{4\Delta u(x,z)}{5\ U_\delta(z_s)}, \tag{14}$$

where $\Delta u\ (x,z)$ is the speed up factor and z_s the upstream height of the considered streamline. Hence, on the hill top

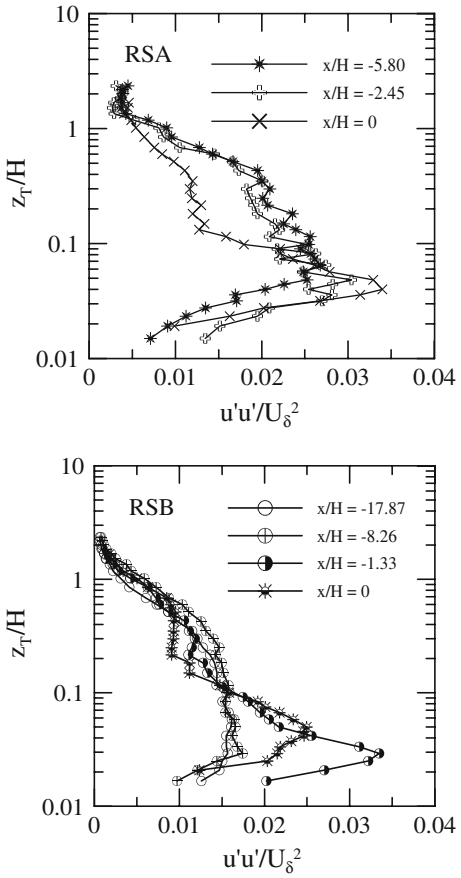

Fig. 10 Normalized longitudinal Reynolds stress profiles upstream of and on the hill top. $z_T = z - d$, z = distance from the bottom of the roughness elements, d = displacement height

$\overline{u'u'}$ decreases and $\overline{w'w'}$ increases in the external flow region.

In contrast, when $T_L \ll T_a$, the dissipation of turbulent kinetic energy acts so fast that local equilibrium is established. This condition is closely satisfied by the flow in the near wall region. Based on estimates for the changes in surface shear stress due to the hill presence, $\Delta\tau$, Britter et al. (1981) assert that $\overline{u'u'}$, $\overline{w'w'}$, $\overline{v'v'}$ increase in proportion to $\Delta\tau/\rho\ u_*^2$.

The changes in Reynolds stresses are shown in Figs. 10 to 18. Upstream of the hill top, in the external flow region, $\overline{u'u'}$ falls as the flow accelerates and shear decreases (Fig. 10). In the near wall region, considering the turbulence production term, $P_{uu} = -2\overline{u'w'}(\partial U/\partial z)$, the large velocity gradients (Fig. 4) give rise to $\overline{u'u'}$ peak values of about 0.035 U_δ^2 for both RSA and RSB conditions. For a smooth wall, Loureiro et al. (2007a) recorded peak values of about 0.023 U_δ^2. On the hill top $\overline{u'u'}$ is observed to decrease in the outer region and increase in the wall region for both RSA and RSB conditions. The trends predicted by Britter et al. (1981) are then verified.

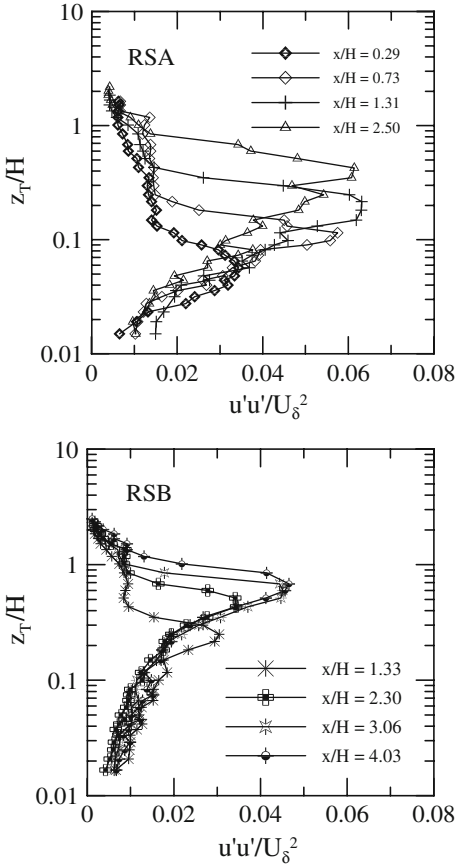

Fig. 11 Normalized longitudinal Reynolds stress profiles on the lee side of hill. $z_T = z - d$, z = distance from the bottom of the roughness elements, d = displacement height

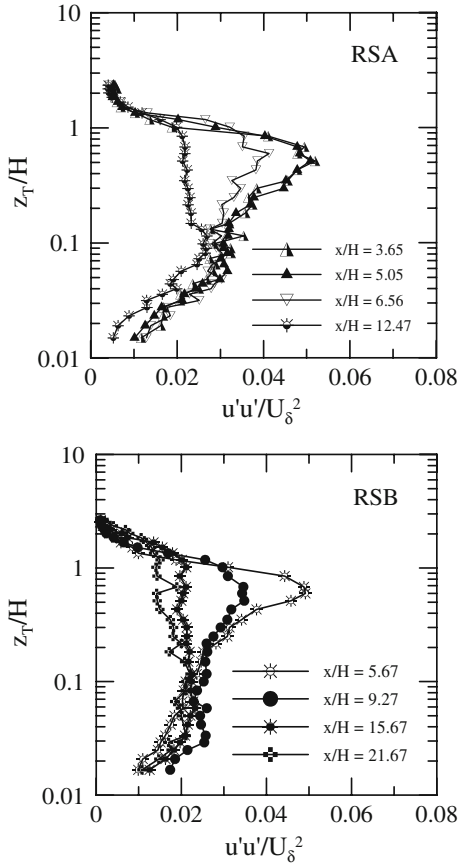

Fig. 12 Normalized longitudinal Reynolds stress profiles downstream of the separation bubble. $z_T = z - d$, z = distance from the bottom of the roughness elements, d = displacement height

The longitudinal Reynolds stress profiles in the separation bubble of the hill are shown in Fig. 11. In this region, turbulence is to a great extent ruled by the free shear layer that bounds the separation region. Turbulence characteristics are hence similar to those of a mixing layer (Wygnanski and Fiedler 1970), with peaks in all turbulent second moments occurring at the points of maximum shear, at about $z_T \approx H$.

The shallow separation bubble for condition RSA implies that flow deceleration increases $\overline{u'u'}$ to a peak value of about 0.06 U_δ^2. The vertical position of peak stress moves away from the wall with increasing x/H, and varies for several profiles from 0.05 H to 0.4 H. For condition RSB, the large separation bubble results in a less pronounced adverse pressure gradient so that the peak value of $\overline{u'u'}$ is 0.047 U_δ^2 and is located at 0.6 H.

In general, lower turbulence levels are observed for condition RSB in comparison to condition RSA. This behaviour can be explained in simple terms by the milder flow deceleration that occurs at RSB condition, which leads to less turbulence production due to lower mean velocity gradients on the lee side of the hill.

Downstream of the separation bubbles (Fig. 12), the peak values of $\overline{u'u'}$ are at their farthest distance from the wall, $z_T \approx 0.6\ H$. As x/H increases the flows slowly relax to equilibrium conditions. Observe that even at position $x/H = 21.67$ (RSB) equilibrium has not yet been achieved.

The large streamwise increase in W and the curvature effects on the upstream side of the hill result in a rise of $\overline{w'w'}$ that is followed by a fall over the hilltop (negative curvature). This trend is clear for condition RSA (Fig. 13). Note the peak value of 0.03 U_δ^2. For condition RSB, the profiles at $x/H = -1.33$ and 0.0 are close together. The peak in $\overline{w'w'}$ is 0.011 U_δ^2.

On the lee side of the hill, the effects of curvature take over adding up to the effects provoked by the shear layer. The result is a very large increase in $\overline{w'w'}$. This combination of effects is particularly relevant for condition RSA (shallow separation bubble) so that the peak value of $\overline{w'w'}$ reaches out to about 0.1 U_δ^2 (Fig. 14). The peak value for condition RSB is 0.04 U_δ^2.

Downstream of the hill, even for the farthest stations, very high values of $\overline{w'w'}$ are observed. The flow is still far from the undisturbed conditions (Fig. 15).

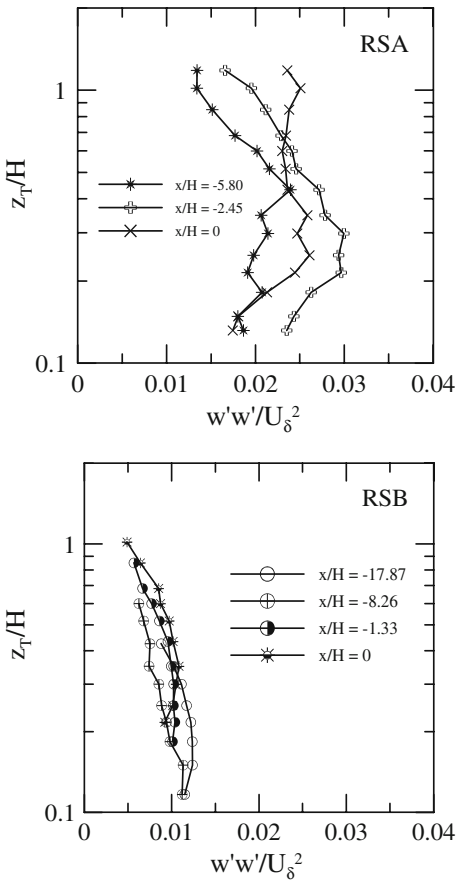

Fig. 13 Normalized transversal Reynolds stress profiles upstream of and on the hill top. $z_T = z - d$, z = distance from the bottom of the roughness elements, d = displacement height

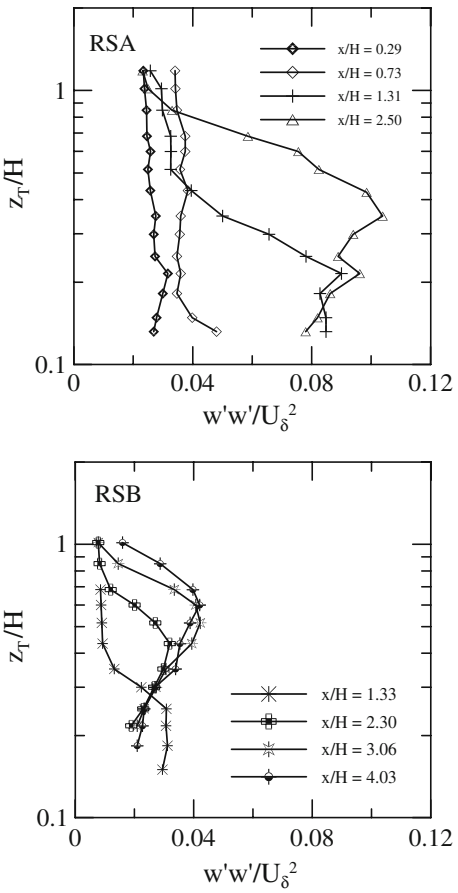

Fig. 14 Normalized transversal Reynolds stress profiles on the lee side of the hill. $z_T = z - d$, z = distance from the bottom of the roughness elements, d = displacement height

The behaviour of the Reynolds shear stress is dominated by curvature. It rises on the upstream side of the hill and falls sharply over the hilltop. This tendency is observed for both conditions (Fig. 16). The peak value for the RSA condition, $-\overline{u'w'} \approx 0.01\ U_\delta^2$ is about twice that for the RSB condition (= 0.005 U_δ^2).

On the lee side of the hill, $-\overline{u'w'}$ is dominated by curvature and shear production. Peak values of 0.037 U_δ^2 and 0.022 U_δ^2 are observed for conditions RSA and RSB, respectively (Fig. 17). The vertical location of both peaks coincides with the location of the peaks for $\overline{u'u'}$ and $\overline{w'w'}$.

Figure 18 illustrates the return of $-\overline{u'w'}$ to equilibrium conditions as the flow proceeds downstream.

4.6.2 The applicability of Eq. 4, mixing length

Equation 4 establishes a linear relation between $\overline{u'w'}$ and $\partial_x p$. Thus, far away from regions where $\partial_x p$ is relevant, a local region where the local shear stress is constant (and approximately equal to u_*^2) should be identified. At a separation point, in contrast, the profile should be linear through origin.

The $\overline{u'w'}$-profiles at stations $x/H = -17.87$ and 1.33 (RSB condition) are shown in Fig. 19. Note that despite the low resolution (only four to seven near wall points could be measured) regions of constant and linear shear stress can be recognized in the former and latter stations, respectively.

Since the derivation of Stratford's solution, Eq. 7, in Sect. 2 resorted to the mixing length concept, it might be instructive at this point to assess the validity of this hypothesis. Figure 20 shows graphs of $-\overline{u'w'}$ against $\zeta = (\varkappa z(\partial_z u))^2$ for positions $x/H = -17.87$ and 1.33 (RSB condition). At the separation point, the mixing length relation is observed to furnish a good representation of the local velocity behaviour provided $\varkappa$ is multiplied by 0.36. Stratford (1959) in his original work had suggested this value to be 0.66. The empirical factor β was inserted by Stratford into his theory to incorporate any effects that the pressure rise may have on the mixing-length. This is the main justification for changing the value of von Karman's constant. The factor β is normally expected to be determined by recourse to experiments. The DNS smooth-wall

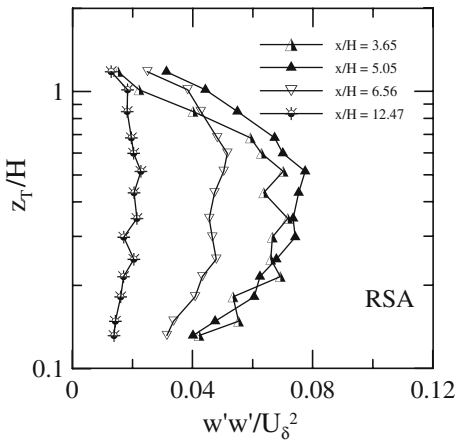

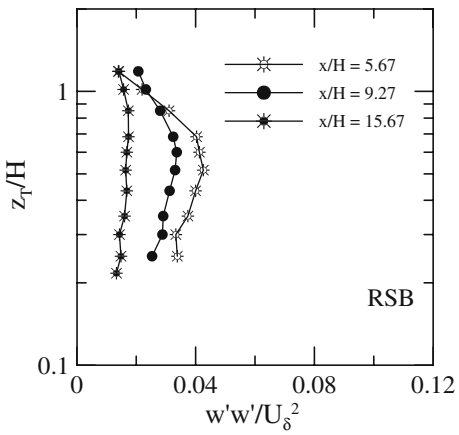

Fig. 15 Normalized transversal Reynolds stress profiles downstream of the separation bubble. $z_T = z - d$, z = distance from the bottom of the roughness elements, d = displacement height

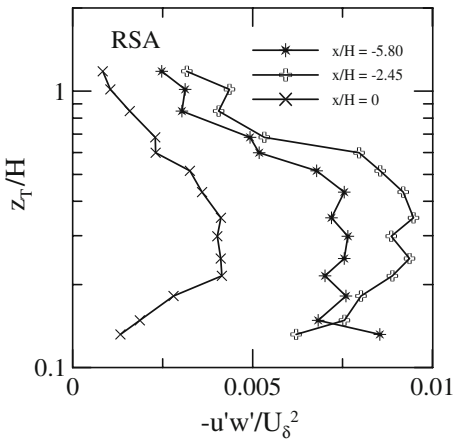

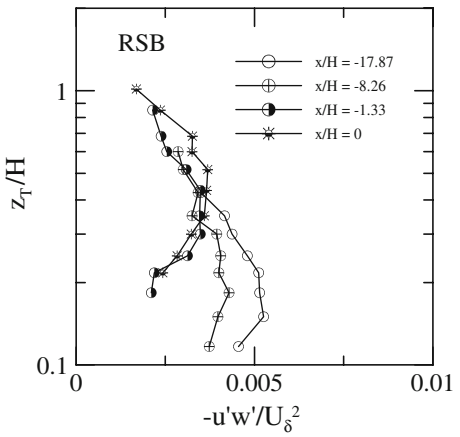

Fig. 16 Normalized Reynolds shear stress profiles upstream of and on the hill top. $z_T = z - d$, z = distance from the bottom of the roughness elements, d = displacement height

data of Na and Moin (1998) give $\beta = 1.18$. More details on the interpretation of β can be found in Stratford (1959).

4.7 Third moments

Important aspects of the previous discussion can be further enlightened by consideration of the higher order moments of the fluctuating velocities. In particular, structural information can be extracted without ambiguity from third and fourth moments (Gad-el-Hak and Bandyopadhyay 1994). The triple velocity products are particularly helpful in separating flow to understand the diffusion process of the Reynolds stresses. The skewness and flatness factors for the longitudinal velocity fluctuations are defined by

$$S_u = \overline{u'^3} / \left(\overline{u'^2}\right)^{3/2}, \tag{15}$$

$$F_u = \overline{u'^4} / \left(\overline{u'^2}\right)^{2}. \tag{16}$$

Equivalent expressions can be written for the other flow properties. A Gaussian distribution satisfies $S_u = 0$ and $F_u = 3$.

4.7.1 General discussion

For flow over a smooth wall, S_u is positive in the near wall region and negative in the external region. Flow regions where S_u is positive are associated with acceleration-dominated velocity fluctuations resulting from the arrival of external high-speed fluid (sweep events) (Gad-el-Hak and Bandyopadhyay 1994). Fernholz and Finley (1996) remark that peak values of $\overline{u'u'}$ lie in the range $13 \leq z^+ (= z\, u_*/\nu) \leq 17$ so that the extremal values for S_u and F_u should also occur in this interval. In the log region, $20 \leq z^+ \leq 500$, S_u and F_u take on the nearly constant values of 0 and 2.8, respectively. The implication is that over a large flow region the velocity fluctuations should follow a nearly Gaussian distribution. Bandyopadhyay and Watson (1988) claim that the general qualitative distributions of S and F are the same for flows over smooth and rough walls, the only significant change being the lower values of S_w (the skewness of the vertical velocity fluctuations) for all rough surfaces.

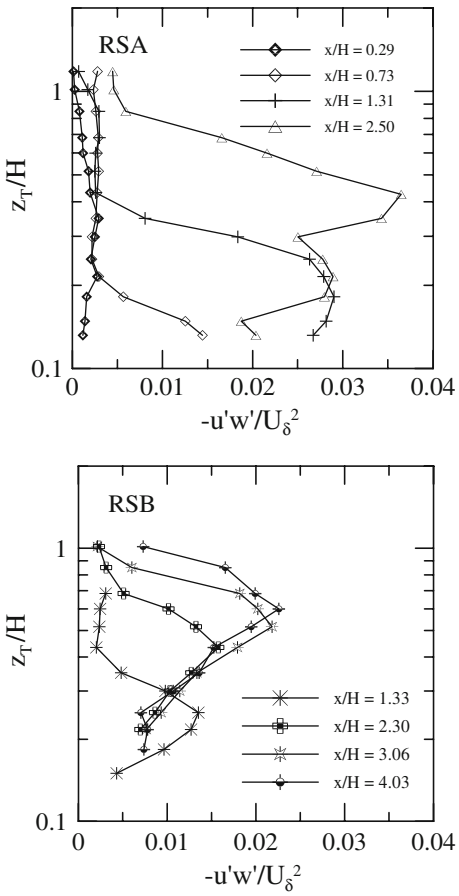

Fig. 17 Normalized Reynolds shear stress profiles in the separation bubble. $z_T = z - d$, z = distance from the bottom of the roughness elements, d = displacement height

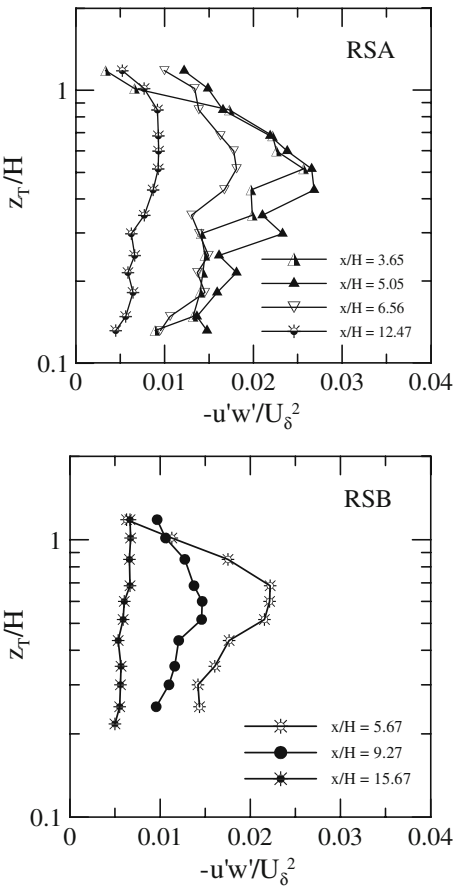

Fig. 18 Normalized Reynolds shear stress profiles downstream of the hill. $z_T = z - d$, z = distance from the bottom of the roughness elements, d = displacement height

The present data show that upstream of and at the hill top, S_u follows the canonical behaviour (Fig. 21). Intense fluctuations are recorded positive near to the wall (≈ 0.5) and negative in the external region (≈ -0.75). It is also apparent that the point of cross-over from positive to negative S_u moves inward as the hill top is approached. At stations $x/H = -17.87$ and -8.26 (RSB), regions of $S_u \approx 0$ can be identified for $0.02 \leq z_T/H \leq 0.3$. In most profiles, S_u dips to negative values, recovers to values near zero, dips again to negative values and returns to near zero values. This oscillating behaviour is particularly apparent for the stations on the hill top. Profiles of skewness with this shape have also been reported by, for example, Andreopoulos et al. (1984).

Downstream of the hill top, the nature of the skewness profiles changes completely (Fig. 22). The S_u profile at $x/H = 0.29$ (RSA) still follows the behaviour described previously. The shallow separation bubble, however, expands largely the region of violent positive fluctuations (e.g., up to $z_T/H \approx 0.4$ for $x/H = 2.5$). After the dip to negative values, no values of S_u close to those of a Gaussian distribution are recorded. For condition RSB, the picture is still clearer. The positive fluctuations increase to the plateau defined by $S_u = 0.5$, dipping sharply to negative values at the free shear layer. No flow region with $S_u = 0$ exists. The three profiles nearest to the separation points ($x/H = 0.73$, RSA; and $x/H = 2.3$, 3.06, RSB) show negative values of S_u very close to the wall.

The large positive fluctuations leaving the region of reverse flow remain for long distances (Fig. 23). Only at station $x/H = 21.67$ (RSB) the S_u profile returns to the canonical shape. Note that for profiles at $x/H = 5.05$ (RSA) and $x/H = 5.67$ (RSB) values of S_u as high as unity are found close to the wall.

Measurements of S_w have been presented by some authors for flow over smooth surfaces. Difficulties related to the spatial and temporal resolution of probes and their large measurement uncertainties make these results differ greatly between each other (Gad-el-Hak and Bandyopadhyay 1994). However, most works agree that the value of

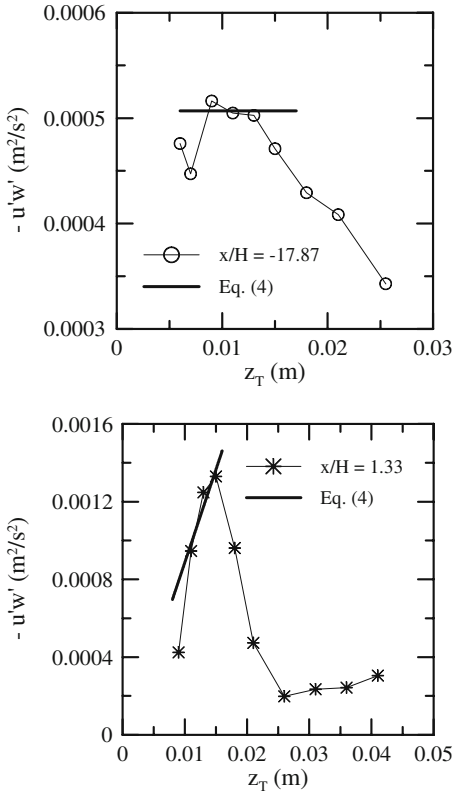

Fig. 19 Shear stress profiles far away and at a separation point. $z_T = z - d$, z = distance from the bottom of the roughness elements, d = displacement height

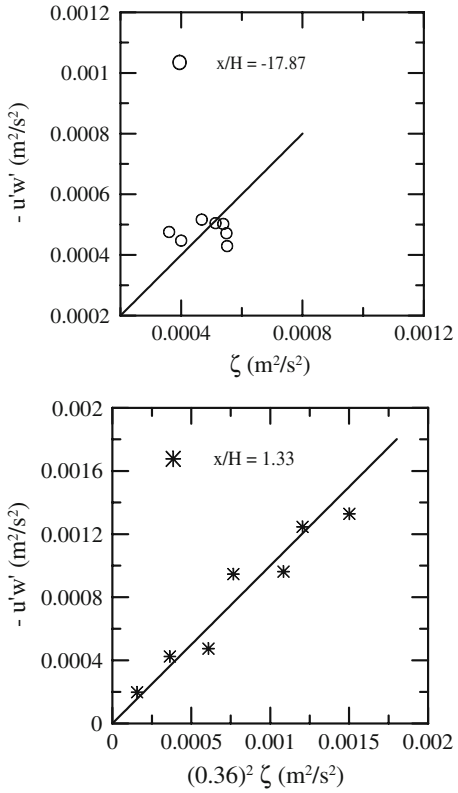

Fig. 20 Mixing length profiles far away and at a separation point $(\zeta = (\kappa z_T(\partial_{z_T} u))^2)$

S_w is negative near the wall and positive in the outer region. In the log-region, S_w remains positive but near zero (≈ 0.1), that is, to a Gaussian distribution. Bandyopadhyay and Watson (1988) found only positive values of S_w over their entire measurement range, for flows over smooth and rough walls.

Here, a small monotonic increase of S_w with x/H is observed upstream the hill top for both rough surface conditions (Fig. 24, only condition RSB shown here). All profiles for the RSA condition show the same trend. At the region of reverse flow, large negative fluctuations of the vertical velocity are seen for the RSB condition (Fig. 25) near the wall. Above this region, vertical fluctuations become positive with peak values of S_w of 0.6 (RSA) and 0.8 (RSB).

4.7.2 Third order closure model

Several transport models for the third moments have been presented in the literature. One of the simplest propositions is that of Daly and Harlow (1970), who postulate

$$\overline{u_i u_j u_k} = \Gamma \tau \overline{u_k u_l} \partial_l(\overline{u_i u_j}) \tag{17}$$

with $\tau = \kappa/\varepsilon$, and $\Gamma = 0.22$ (smooth wall).

This expression has been tested in Fig. 26 for the longitudinal third moment. Two positions are considered: $x/H = -17.87$ and 1.33 (RSB condition). Please note the very distinct behaviour of S_u far away and near to a separation point. We had previously mentioned that at $x/H = -17.87$ S_u has a very high value near the wall, dips continuously to a negative peak value and recovers to zero on moving away from the wall. At the separation position, S_u is observed to vary much more violently. Starting from zero at the wall, S_u increases to a maximum value, dips sharply to a negative peak value and recovers quickly again to about zero. Despite the differences, Eq. 17 is observed to match very well the experiments. The near wall behaviour of S_u is particularly well represented at $x/H = 1.33$.

For flow over a rough surface, the multiplying constant Γ was found to be 1.1. For attached flow over rough surfaces S_u is recognized to yield near wall values of 0.5 (Krogstad and Antonia 1999; Flack et al. 2007, present work). This result is consistent with $\Gamma = 1.1$.

4.8 Fourth moments

Profiles for the flatness in a boundary layer show very high values near the wall and in the outer layer, where

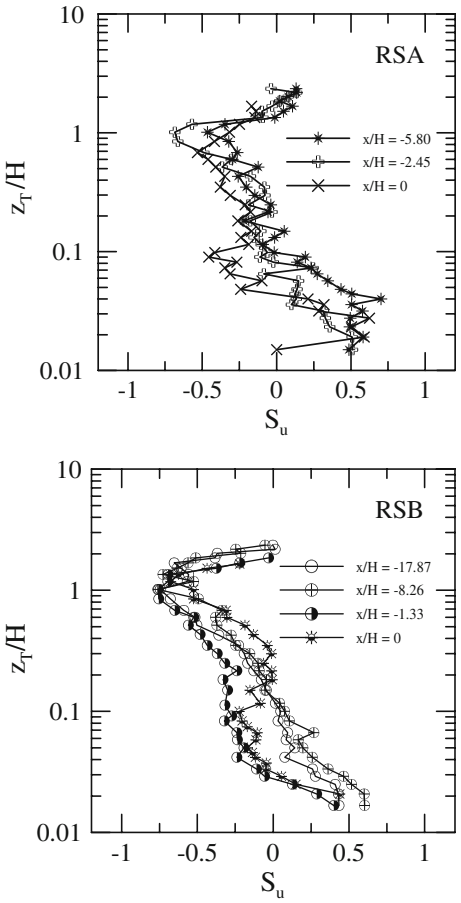

Fig. 21 Skewness factor of longitudinal velocity fluctuations upstream of and on the hill top. $z_T = z - d$, z = distance from the bottom of the roughness elements, d = displacement height

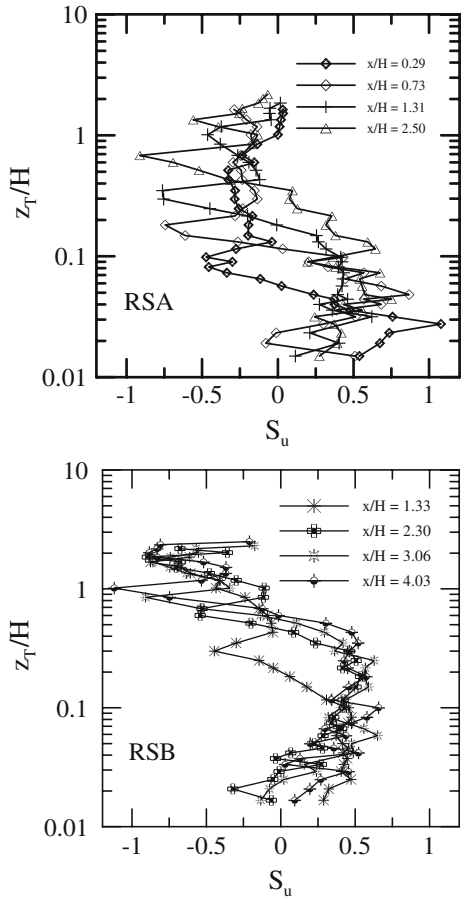

Fig. 22 Skewness factor of longitudinal velocity fluctuations in the separation bubble. $z_T = z - d$, z = distance from the bottom of the roughness elements, d = displacement height

turbulence is highly intermittent. In the log-region, $F_u \approx 2.8$, as mentioned before.

Profiles of F_u are show in Fig. 27 for the upstream side of the hill. As the flow accelerates to the hill top the longitudinal fluctuations become less intermittent near the wall. Then, over the top, fluctuations become highly irregular again (see position $x/H = 0$, RSB-flow, $0.01 \leq z_T/H \leq 0.1$, so that $F_u = 3.3$). In the outer regions of the RSA- and RSB-flows, $F_u \approx 2.8$ and 3.0, respectively, so that the distributions are nearly Gaussian.

On the lee side of the hill (Fig. 28), the shallow separation bubble of RSA promotes highly intermittent motions that persist up to $z_T/H \approx 0.1$ (peak value of 5.5). Farther from the wall, F_u oscillates violently but around 3.5. For condition RSB, the picture is much different. The fluctuations are highly intermittent all across the flow except for $z_T/H \approx 1$, the position of the free shear layer. Downstream of the hill, all flatness profiles (not shown here) nearly coincide after position $x/H = 6.56$, with $F_u = 2.8$ in the outer layer.

The distribution of the flatness of the vertical velocity fluctuations, F_w, for condition RSA is Gaussian ($F_w = 3.0$) on the upstream side of the hill (figures not shown here) and on the hill top, $F_w = 3.25$. For condition RSB, all profiles satisfy $F_w = 3.4$, increasing to about $F_w = 4$ in the outer region. On the lee side of the hill, the disturbances caused by the separation bubbles increase the scatter in F_w. For conditions RSA and RSB, F_w is noted to vary between 2.5 and 3.5 for all profiles with peaks of 5.6 for position $x/H = 4.03$. Downstream of the hill, F_w varies between 3.1 (RSA-profiles) and 3.5 (RSB-profiles).

5 Final remarks

The present work is a necessary complement to the work of Loureiro et al. (2007a). In that work, flow over a steep, smooth hill was studied with the purpose of providing reference data for the validation of asymptotic theories and numerical simulations. Thus, a particular emphasis was

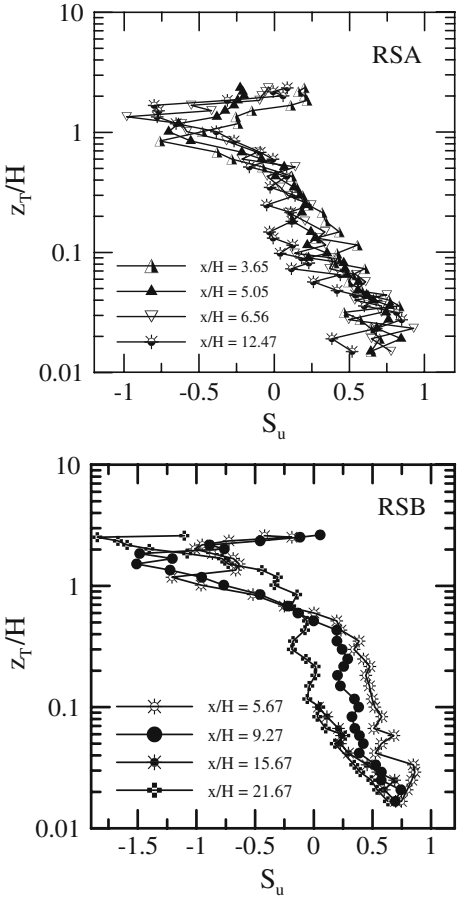

Fig. 23 Skewness factor of longitudinal velocity fluctuations downstream of the hill. $z_T = z - d$, z = distance from the bottom of the roughness elements, d = displacement height

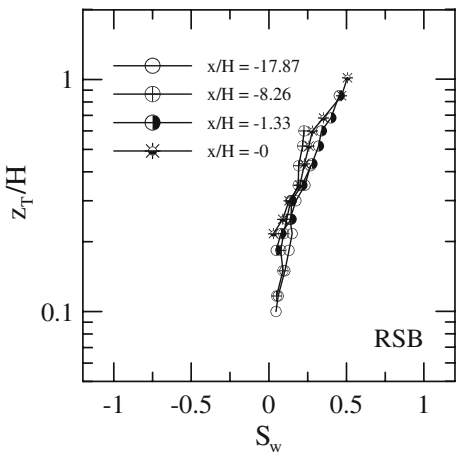

Fig. 24 Skewness factor of vertical velocity fluctuations upstream of and on the hill top. $z_T = z - d$, z = distance from the bottom of the roughness elements, d = displacement height

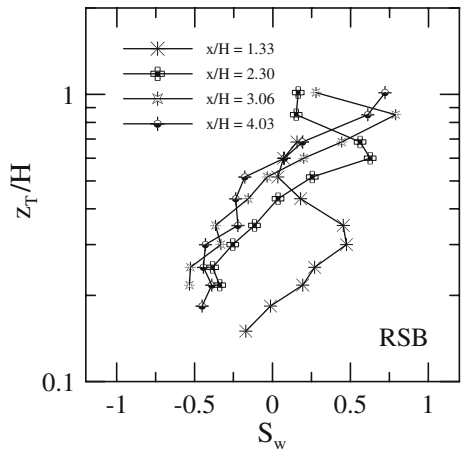

Fig. 25 Skewness factor of vertical velocity fluctuations in the separation bubble. $z_T = z - d$, z = distance from the bottom of the roughness elements, d = displacement height

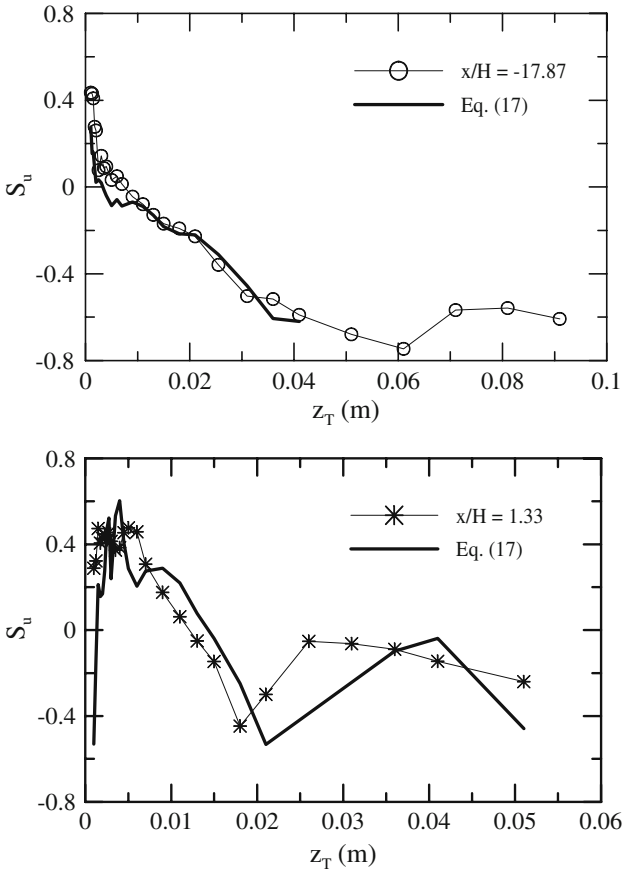

Fig. 26 Skewness factor of longitudinal velocity fluctuations far away and at a separation point. $z_T = z - d$, z = distance from the bottom of the roughness elements, d = displacement height

placed in the accurate determination of the wall shear stress, which was evaluated from polynomial fits to the near wall mean velocity data.

Here, two extra flow conditions were experimentally studied. These conditions consider flow over a rough surface and the same hill geometry but different external

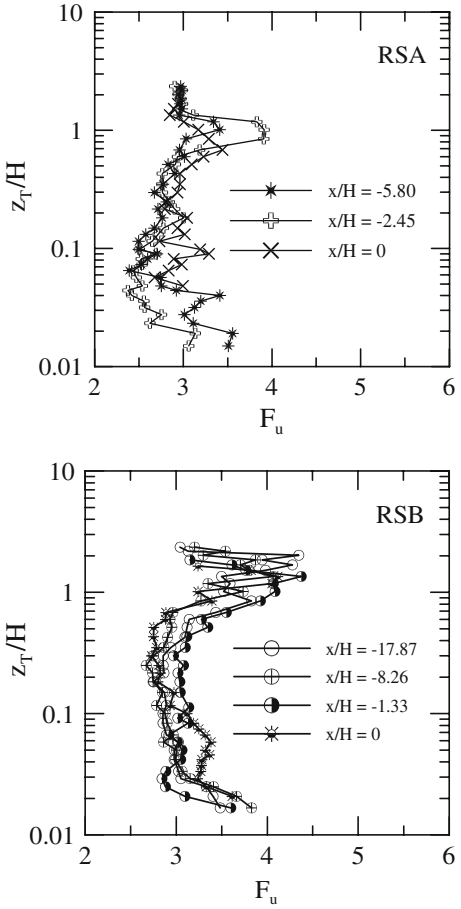

Fig. 27 Flatness factor of longitudinal velocity fluctuations upstream of and on the hill top. $z_T = z - d$, z = distance from the bottom of the roughness elements, d = displacement height

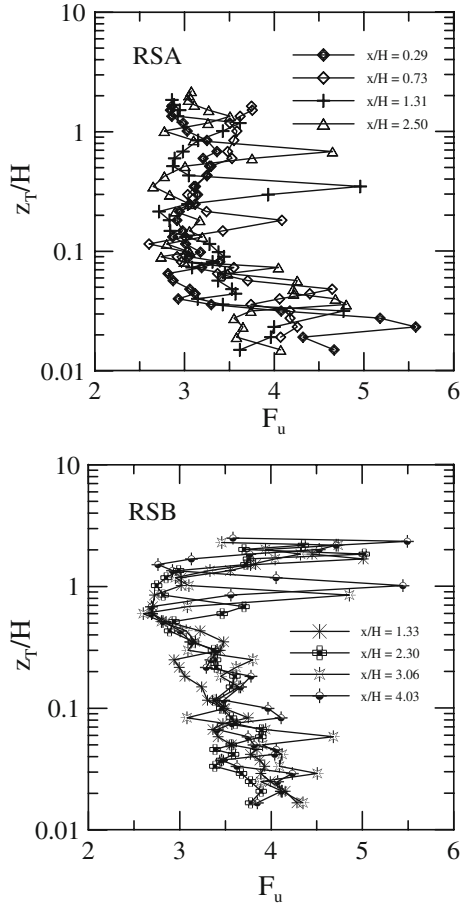

Fig. 28 Flatness factor of longitudinal velocity fluctuations in the separation bubble. $z_T = z - d$, z = distance from the bottom of the roughness elements, d = displacement height

flow conditions. Considering the thirteen measurement stations of Loureiro et al. (2007a, b) for smooth wall, the complete set of data for smooth and rough walls encompasses 36 stations. This body of data provides a detailed account of flows with separation, furnishing reference data that can be used to validate proposed models for separated flow.

Results on two-component mean flow velocities and higher-order statistical quantities were presented. These results allowed the development of a new parametrization for rough wall boundary layers and validated the use of Stratford's solution for a separating rough flow. Data for the shear and normal components of the Reynolds stress tensor and the distributions of skewness and flatness factors for the streamwise and vertical velocity fluctuations were thoroughly analised. In particular, the behaviour of the shear stress, the mixing-length and a third order closure model were investigated for a rough wall separation point.

Acknowledgments JBRL benefited from a Research Fellowship from the Brazilian Ministry of Science and Technology through Programme Prometro (Grant no. 554391/2006-6). ASM benefited from a Research Scholarship from the Brazilian National Research Council (CNPq). ASM is also thankful to the Rio de Janeiro Research Foundation (FAPERJ) (Grant no. E-26/171.198/2003) for the concession of further financial help regarding his stay at Oporto University. APSF is grateful to the Brazilian National Research Council (CNPq) for the award of a Research Fellowship (Grant no. 306977/2006-0). The work was financially supported by CNPq through Grants no. 477392/2006-7 and no. 476091-2007/1, and by the Rio de Janeiro Research Foundation (FAPERJ) through Grants E-26/171.346/2005 and E-26/171.198/2003. ASM, JBRL and FTP are grateful to Prof. Maria Fernanda Proença of the Hydraulics Laboratory of Oporto University for all her help in setting up the flow rig, as well as for some very interesting technical discussions.

References

Allen B, Brown AR (2002) Large-eddy simulation of turbulent separated flow over rough hills. Bound Layer Meteorol 102:177–198

Andreopoulos J, Durst F, Zaric Z, Jovanovic J (1984) Influence of Reynolds number on characteristics of turbulent wall boundary layers. Exp Fluids 2:7–16

Arya SPS, Gadiyaram PS (1986) An experimental study of flow and dispersion in the wakes of three-dimensional low hills. Atmos Environ 20:729–740

Bandyopadhyay PR, Watson RD (1988) Structure of rough-wall turbulent boundary layer. Phys Fluids 31:1877–1883

Batchelor G, Proudman I (1954) The effect of rapid distortion of a fluid in turbulent motion. Q J Mech Appl Math 7:83-103

Britter RE, Hunt JCR, Richards KJ (1981) Air flow over a two-dimensional hill: studies of velocity speedup, roughness effects and turbulence. Q J R Meteorol Soc 107:91–110

Brown AR, Hobson JM, Wood N (2001) Large-eddy simulation of neutral turbulent flow over rough sinusoidal ridges. Bound Layer Meteorol 98:411–441

Bush WB, Fendell FE (1972) Asymptotic analysis of turbulent channel flow and boundary layer flow. J Fluid Mech 56:657–681

Castro IP (2007) Rough-wall boundary layers: mean flow universality. J Fluid Mech 585:469–485

Castro IP, Apsley DD (1997) Flow and dispersion over topography: a comparison between numerical and laboratory data for two-dimensional flows. Atmos Environ 31:839–850

Cruz DOA, Silva Freire AP (1998) On single limits and the asymptotic behaviour of separating turbulent boundary layers. Int J Heat Mass Transf 41:2097–2111

Daly JR, Harlow IH (1970) Transport equations in turbulence. Phys Fluids 13: 2634–2649

Durbin PA, Belcher SE (1992) Scaling of adverse-pressure-gradient turbulent boundary layers. J Fluid Mech 238: 699–722

Fernholz HH, Finley PJ (1996) The incompressible zero-pressure-gradient turbulent boundary layer: an assessment of the data. Prog Aero Sci 32:245–311

Flack KA, Schultz MP, Connely JS (2007) Examination of a critical roughness height for outer layer. Phys Fluids 19:95–104

Gad-el-Hak M, Bandyopadhyay PR (1994) Reynolds number effects in wall-bounded turbulent flows. Appl Mech Rev 47:307–365

Goldstein S (1948) On laminar boundary layer flow near a position of separation. Q J Mech Appl Maths 1:43–69

Hewer BJ (1998) Non-linear numerical model predictions of flow over an isolated hill of moderate slope. Bound Layer Meteorol 87:381–408

Hunt JCR, Leibovich S, Richards KJ (1988) Turbulent shear flow over low hills. Q J Roy Meteorol Soc 114:1435–1470

Iizuka S, Kondo H (2004) Performance of various sub-grid scale models in large-eddy simulations of turbulent flow over complex terrain. Atmos Environ 38:7083–7091

Ishihara T, Fujino Y, Hibi K (2001) Wind tunnel study of separated flow over a two-dimensional ridge and a circular hill. J Wind Eng 89:573–576

Jackson PS, Hunt JCR (1975) Turbulent wind flow over a low hill. Q J R Meteorol Soc 101:929–955

Kaimal JC, Finnigan JJ (1994) Atmospheric boundary layer flows. Oxford University Press, Oxford

Kim HG, Lee CM, Lim HC, Kyong NH (1997) An experimental and numerical study on the flow over two-dimensional hills. J Wind Eng Ind Aero 66:17–33

Krogstad PA, Antonia RA (1999) Surface roughness effects in turbulent boundary layers. Exp Fluids 27:450–460

Lighthill J (1986) An informal introduction to theoretical fluid mechanics, C.U.P

Loureiro JBR, Pinho FT, Silva Freire AP (2007a) Near wall characterization of the flow over a two-dimensional steep smooth hill. Exp Fluids 42:441–457

Loureiro JBR, Soares DV, Fontoura Rodrigues JLA, Pinho FT, Silva Freire AP (2007b) Water tank and numerical model studies of flow over steep smooth two-dimensional hills. Bound Layer Meteorol 122:343–365

Mellor GL (1966) The effects of pressure gradients on turbulent flow near a smooth wall. J Fluid Mech 24:255–274

Mellor GL (1972) The large Reynolds number, asymptotic theory of turbulent boundary layers. Int J Eng Sci 10:851–873

Na Y, Moin P (1998) Direct numerical simulation of a separated turbulent boundary layer. J Fluid Mech 374:379–405

Nakayama A, Koyama H (1984) A wall law for turbulent boundary layers in adverse pressure gradients. AIAA J 22:1386–1389

Perry AE, Joubert PN (1963) Rough-wall boundary layers in adverse pressure gradients. J Fluid Mech 17:193–211

Perry AE, Schofield WH, Joubert PN (1969) Rough-wall turbulent boundary layers. J Fluid Mech 37:383–413

Prandtl L (1925) Über die ausgebildete Turbulenz. ZAMM 5:136–139

Ross AN, Arnold S, Vosper SB, Mobbs SD, Nixon N, Robins AG (2004) A comparison of wind-tunnel experiments and numerical simulations of neutral and stratified flow over a hill. Bound Layer Meteorol 113:427–459

Simpson RL (1996) Aspects of turbulent boundary-layer separation. Prog Aero Sci 32:457–521

Snyder WH, Castro IP (2002) The critical Reynolds number for rough-wall boundary layers. J Wind Eng Ind Aerodyn 90:41–54

Stratford BS (1959) The prediction of separation of the turbulent boundary layer. J Fluid Mech 5:1–16

Sychev VV, Sychev Vik V (1980) On turbulent separation. USSR Comput Maths Math Phys 20:133–145

Sykes RI (1980) An asymptotic theory of incompressible turbulent boundary-layer flow over a small hump. J Fluid Mech 101:647–670

Townsend AA (1976) The structure of turbulent shear flow, C.U.P.

Wygnanski I, Fiedler HE (1970) The two-dimensional mixing region. J Fluid Mech 41:327–361

Yajnik KS (1970) Asymptotic theory of turbulent shear flow. J Fluid Mech 42:411–427

Ying R, Canuto VM (1997) Numerical simulation of the flow over two-dimensional hills using a second-order turbulence closure model. Bound Layer Meteorol 85:447–474